

# Energy deposition dynamics of femtosecond pulses in water

Stefano Minardi,<sup>1, a)</sup> Donatas Majus,<sup>2</sup> Amrutha Gopal,<sup>3</sup> Gintaras Tamošauskas,<sup>2</sup> Carles Milián,<sup>4</sup> Arnaud Couairon,<sup>4</sup> Thomas Pertsch,<sup>1</sup> and Audrius Dubietis<sup>2</sup>

<sup>1)</sup> Institute of Applied Physics, Friedrich-Schiller-Universität Jena, Max-Wien-Platz 1, 07743 Jena, Germany

<sup>2)</sup> Department of Quantum Electronics, Vilnius University, Sauletekio 9, bldg. 3, LT-10222 Vilnius, Lithuania

<sup>3)</sup> Institute of Optics and Quantum Electronics, Friedrich-Schiller-Universität Jena, Max-Wien-Platz 1, 07743 Jena, Germany

<sup>4)</sup> Centre de Physique Théorique, CNRS, École Polytechnique, F-91128 Palaiseau, France

(Dated: 2 January 2019)

We exploit inverse Raman scattering and solvated electron absorption to perform a quantitative characterization of the energy loss and ionization dynamics in water with tightly focused near-infrared femtosecond pulses. A comparison between experimental data and numerical simulations suggests that the ionization energy of water is 8 eV, rather than the commonly used value of 6.5 eV.

Keywords: Inverse Raman Scattering, light matter interaction, cold plasma

Femtosecond laser pulses tightly focused in dielectric media have a wide range of applications in science and technology. Because of their capability to deposit high ionization doses in volumes of a few cubic microns, they can be used to induce permanent, microscopic refractive index modification in solid dielectrics, thus enabling three-dimensional integrated optics<sup>1,2</sup>. By focusing femtosecond pulses in liquids, it is possible to induce localized chemical reactions such as photo-polymerization on the micro-nano-scale<sup>3</sup>. In aqueous media, such as biological tissues, tightly focused femtosecond laser pulses have been successfully employed for eye surgery<sup>4</sup> and treatment of cancerous cells<sup>5</sup>. Recent studies show the control on the input chirp provides an effective control on the energy deposition in water<sup>6</sup>. Future developments of these applications will benefit from a more advanced control of the energy deposition by means of arbitrarily spatiotemporally tailored laser wavepackets<sup>7</sup>. In this context, suitable diagnostic tools for real time analysis of energy deposition dynamics as well as a better understanding of the initial stages of the energy absorption in the dielectric medium are of foremost importance.

In previous experiments based on quantitative shadowgraphy, we characterized the propagation of a 120 fs pulse focused with low NA in water<sup>8,9</sup>. In this configuration, the laser pulse enters a filamentation regime<sup>10</sup> leaving behind a tenuous, few-mm-long plasma channel which gets solvated on a ps timescale. The pulse dynamics (featuring pulse splitting and superluminal pulse formation) was clearly seen in the probe as an absorption feature, which we attributed to the imaginary part of an unspecified cross-phase modulation process (XPM) between pump and probe.

Here we explore the energy deposition dynamics of

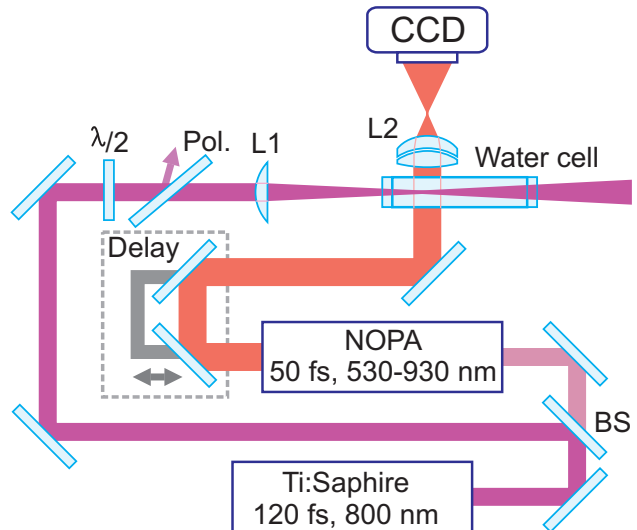


FIG. 1. The experimental set-up.  $\lambda/2$ : rotating lambda-half plate. Pol.: polarizer. L1: pump focusing lens (NA 0.08). L2: microscope objective (NA 0.25).

tightly focused near infrared pulses in water. We provide experimental evidence that the previously reported XPM absorption of the weak probe pulse is in fact inverse Raman scattering (IRS)<sup>11</sup>, allowing us to exploit single shadowgrams to extract the peak intensity, power and the pulse duration of the pump and their evolution on microscopic propagation lengths. By combining these data with the peak plasma density estimated from the absorption traces of solvated electrons, we have reconstructed the energy loss dynamics of the pump pulse.

A scheme of the setup is depicted in Figure 1. The 120 fs pulse from the Ti:Sapph laser is split among two channels. One channel (the pump) is focused by lens L1 at  $NA = W_{1/e^2}/f \sim 0.08$  in the middle of a quartz cuvette filled with purified water ( $W_{1/e^2}$  is the waist radius

<sup>a)</sup> Electronic mail: stefano@stefanominardi.eu; http://stefanominardi.eu.

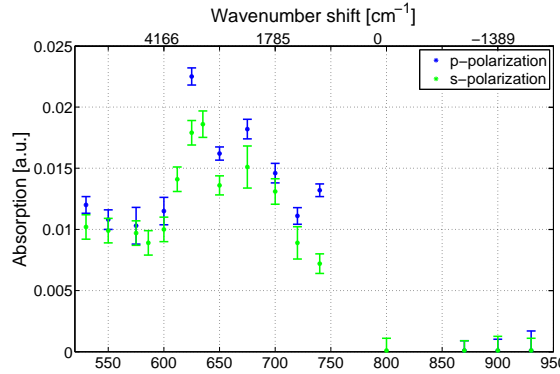


FIG. 2. Absorption spectrum of the shadow of the pump pulse. Peak absorption is found at  $\lambda_{\text{probe}} = 625$  nm, which corresponds to a detuning of  $3500\text{ cm}^{-1}$  from the pump frequency ( $\lambda_{\text{pump}} = 800$  nm).

of the Gaussian beam). The energy of the pump beam is regulated by a  $\lambda/2$  plate and polarizer to  $810 \pm 5$  nJ, so that a stable,  $\sim 200\text{ }\mu\text{m}$ -long channel of solvated electrons can be excited. Energy of the pump was kept below the threshold for broadband supercontinuum generation and cavitation bubble formation<sup>12</sup>. The second channel (probe) consists of 50 fs pulses tunable from 530 to 930 nm and delivered by a second-harmonic-pumped non-collinear optical parametric amplifier (NOPA) (Topas White - Light Conversion Ltd.). The probe beam is collimated and illuminates the cuvette perpendicular to the direction of propagation of the pump. A long working distance microscope equipped with a high-resolution CCD camera is then used to record the transmitted beam profile with a transverse spatial resolution of  $2\text{ }\mu\text{m}$  and a plate scale of  $0.5\text{ }\mu\text{m}/\text{pixel}$ . The focal plane of the microscope is set on the plane containing the channel so that only transmission measurements are possible with the shadowgram.

Initially, we studied the spectral characteristics of the absorption features appearing in the shadowgrams, by recording a sequence of instant images (taken by scanning the delay of the probe in steps of 50 fs) of the focusing pump pulse for 17 probe wavelengths between 530 and 930 nm. We noticed that for a fixed position in space and probe wavelength shorter than 740 nm, the time profile of the absorption signal was characterized by a sharp peak ( $\sim 100\text{-}150$  fs duration) followed by a slowly growing signal (time constant 500 fs). In previous experiments with  $\lambda_{\text{probe}} = 560$  nm (Ref. 8), we interpreted this feature as a signature of the pump pulse followed by the buildup of the solvation of a free-electron plasma. On the contrary, for probe wavelengths larger than 740 nm, only the solvation curve was observed and no signature of the pump pulse was evident. By measuring the peak absorption of the pump pulse feature as a function of the probe wavelength we obtained the spectrum depicted in Fig. 2. The spectrum is peaked at  $\lambda_{\text{probe}} = 625$  nm and its profile is

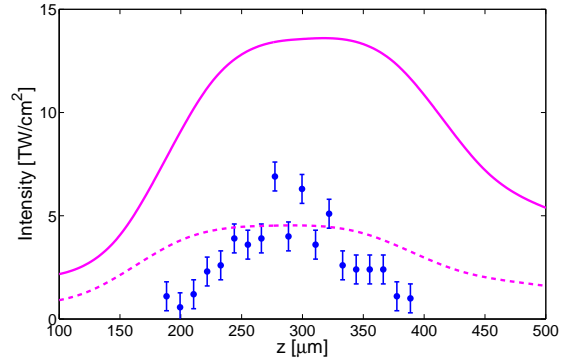


FIG. 3. Dots: Measured peak intensity as a function of the propagation distance obtained by analyzing shadowgrams at  $\lambda_{\text{probe}} = 625$  nm. The results are compared to the on-axis numerical peak intensity averaged over the probe pulse duration (full line). The rescaled simulation data (broken line) show a good agreement of the shape of the plot with experimental data.

insensitive to the polarization state of the probe beam. A similar spectral feature has been previously observed in supercontinuum spectra of filaments in water<sup>13</sup> and attributed to IRS<sup>11</sup>. Indeed, the frequency difference between the probe and the pump corresponds precisely to the well known vibrational frequency at  $\nu \sim 3500\text{ cm}^{-1}$  of the hydroxyl bond stretching<sup>14</sup>. The shadowgraphic signal  $F_{\text{shad},t}(x,z)$  at  $\lambda_{\text{probe}} = 625$  nm due to the IRS can be written as<sup>15</sup>:

$$F_{\text{shad},t}(x,z) = F_{\text{probe}} \exp \left[ -g \int I_{\text{pump}}(x,y,z,t) dy \right], \quad (1)$$

where  $F_{\text{probe}}$  is the fluence of the plane wave, impulsive probe crossing the pump pulse of intensity  $I_{\text{pump}}(x,y,z,t)$  at time  $t$  (laboratory frame). The constant  $g$  is the Raman gain which, for the transition at  $\nu \sim 3500\text{ cm}^{-1}$ , takes the value of  $0.14\text{ cm/GW}$  (Ref. 16). For finite probe pulse duration,  $I_{\text{pump}}$  should be read as the peak intensity averaged over the probe duration<sup>17</sup>. We analyzed the shadowgrams following two different procedures. From one side, we exploited the radial symmetry of the pump beam to perform the Abel inversion of the absorbance ( $A = -\log_{10} T$ , where  $T = F_{\text{shad},t}(x,z)/F_{\text{probe}}$ , Ref. 18) and extract the on-axis peak intensity of the pump pulse according to Eq. (1). On the other side, we integrated in space the absorbance signal to retrieve the power profile of the pump pulse.

The measured intensities at the position  $z$  of the pulse peak (the propagation coordinate of the pulse) are depicted in Fig. 3. We notice that the peak intensities at their maximum exceed  $5\text{ TW/cm}^2$ , highlighting that tunneling ionization starts to play a significant role in the excitation process of the water molecules (Keldysh parameter  $\gamma < 2.7$  for a gap energy of  $U_g = 6.5\text{ eV}$ , Refs. 19 and 20). This observation lead us to choose a Keldysh

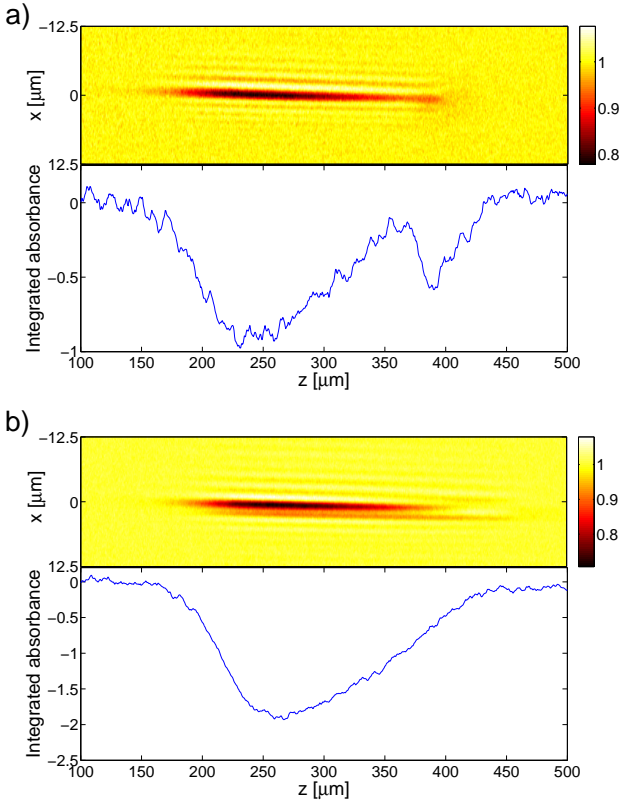


FIG. 4. (a) Top: Original shadowgram at  $\lambda_{\text{probe}} = 625 \text{ nm}$  after noise removal by local averaging with a  $1 \mu\text{m} \times 1 \mu\text{m}$  stencil. The propagation direction of the pulse is from left to right. Bottom: Absorbance integrated along the  $x$  coordinate for the same shadowgram. (b) Top: The corresponding shadowgram at  $\lambda_{\text{probe}} = 800 \text{ nm}$ . Notice that both the shadowgram and the integrated absorbance (bottom) do not show any trace of the pump pulse.

rate model for the ionization in the numerical simulation.

An example of the power profile diagnostic is depicted in Fig. 4. The integrated absorbance profile shows a short peak at  $z = 400 \mu\text{m}$  (the pump pulse shadow) followed by the onset of the absorption of the solvated electrons peaked at  $z = 250 \mu\text{m}$ . By measuring the depth, width and position of the peak of the short pulse as a function of the time delay of the frames taken at  $\lambda_{\text{probe}} = 625 \text{ nm}$ , we obtained estimates of the pulse power loss, duration and velocity along propagation. We found that the pulse peak power is traveling at a constant speed of  $v = 0.2227 \pm 0.0012 \mu\text{m}/\text{fs}$ , in excellent agreement with expectations ( $0.2230 \mu\text{m}/\text{fs}$ ). The peak power as a function of the propagation distance has been observed to be approximatively constant and then decay to a value of  $\sim 70\%$  of the initial value along propagation. Pulse duration is also approximatively constant with a FWHM of 120 fs. By combining the data on the pulse duration with the peak power, we can estimate the energy content of the wavepacket as a function of the propagation of the pump pulse (see Fig. 5 (a)).

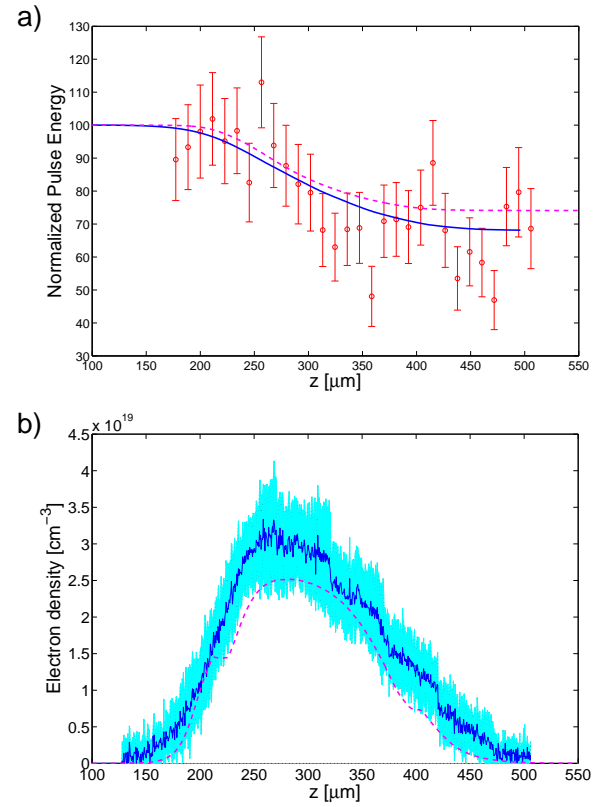


FIG. 5. (a) Spatially resolved energy deposition in the water cuvette. Points: estimated of the losses from the analysis of the IRS traces of the optical pulse. Continuous line: losses estimated from the integration of the measured electron density profile. Dashed line: energy losses as from the numerical simulation of the experiment. (b) Measured solvated plasma density. The shade indicates the error bar interval of our estimate. Dashed line: estimated solvated plasma density from the numerical simulation.

To verify the trend of the energy loss, we analyzed quantitatively the absorption data of the solvated electrons tail. By Abel inversion of the absorbance at  $\lambda_{\text{probe}} = 625 \text{ nm}$  of 5 images taken at a late delay (few hundreds of fs after the pump pulse transit), we obtained the radial distribution of the absorption coefficient. This was related to a solvated electron density by using the known peak decadic molar extinction coefficient ( $\epsilon_{720} = 1.85 \times 10^4 \text{ cm}^{-1} \text{ mol}^{-1} \text{ dm}^3$ , Ref. 21) suitably scaled to the wavelength of 625 nm from the absorption spectrum of the plasma channel ( $\epsilon_{625} = 1.32 \times 10^4 \text{ cm}^{-1} \text{ mol}^{-1} \text{ dm}^3$ ), which we measured (data not shown). The peak solvated plasma density as a function of the propagation length  $z$  is depicted in Fig. 5(b). The plasma channel had a uniform FWHM diameter of  $3.0 \pm 0.5 \mu\text{m}$ .

Numerical simulations were carried out to have more insight in the energy deposition process. To this end we used a model for nonlinear pulse propagation in the presence of plasma. The pulse propagation is described by a Unidirectional Nonlinear Envelope Equation<sup>22</sup> in

cluding sources accounting for Kerr self-focusing ( $n_2 = 2.7 \times 10^{-16} \text{ cm}^2/\text{W}$ ), plasma defocusing and nonlinear losses due to plasma formation and plasma absorption. This equation is solved together with a rate equation for the plasma density, which includes excitation of electrons using the Keldysh ionization rate<sup>19</sup>, as well as recombination with time  $\tau_r = 100 \text{ fs}$  (Ref. 9). The plasma is modeled as a Drude gas, so that the inverse Bremsstrahlung cross section is proportional to the plasma resistivity regulated by a single parameter  $\tau_c = 3 \text{ fs}$ , describing the collision time of the plasma. The pulse parameters are fixed (NA=0.072, pulse duration 120 fs and energy 810 nJ). To convert the plasma density in the solvated electron density, we considered a scenario in which the quantum yield of the solvated electrons depends on the total energy of the multi-photon transition responsible for the excitation of a free electron<sup>23</sup>. In the simulation, we used a ionization potential of 8 eV, which is considered as the correct ionization potential of water, according to recent literature<sup>24</sup>. It corresponds to a total transition of 9.24 eV, and a solvation yield of 44%. Note that the standard value of 6.5 eV (Ref. 20), corresponding to a total transition energy of 7.7 eV and a fraction of only 4% of solvated electrons, did not allow us to reproduce quantitatively the solvated electron density and absorption simultaneously. In contrast, with a gap of 8 eV, we were able to fit precisely both the measured solvated electron curve and the energy losses (see Fig. 5). By post-processing the measurement data of the plasma distribution and assuming that a 6-photon process is required to excite one molecule, we obtained a loss curve which nicely fits the loss data obtained from the measurements using IRS shadows, provided we further assume that only 50% of the produced excitations form a solvated electron (see Fig. 5(a)). Despite these good agreements, simulations were able to reproduce only within a factor 2-3 the measured average peak intensities as a function of the propagation length (Fig. 3). Possible causes of the mismatch between the observed intensities and the numerical data could be an overestimate of the Raman gain we used to retrieve the experimental data and the blurring associated to the finite spatial resolution of our microscope objective.

Concluding, we showed that by tuning the probe wavelength to the Raman shifted wavelength, intense optical pulses propagating in condensed matter dielectrics can be visualized as transmission dips in shadowgrams. Simultaneously, the single shadowgram can provide information on the plasma density, if some form of color-center can be generated after the relaxation of the electrons. In our water samples we were able to combine the information about the spatiotemporal dynamics the pump pulse

with a precise estimate of the deposited energy. Our numerical investigation combined with experimental findings pointed out that the relevant ionization process for a  $\lambda_0 = 800 \text{ nm}$  pump is a 6-photon-absorption, confirming that the ionization potential of water is  $U_g \sim 8 \text{ eV}$ .

S.M. and A.G. acknowledge financial support from European Commission Seventh Framework Programme project LASERLAB-EUROPE access, Grant No. 228334. D.M., G.T. and A.D. acknowledge financial support from the European Social Fund under the Global Grant measure (Grant No. VP1-3.1-ŠMM-07-K-03-001). A.C. and C.M. acknowledge financial support from the French DGA.

- <sup>1</sup>T. Pertsch, U. Peschel, F. Lederer, J. Burghoff, M. Will, S. Nolte, and A. Tünnermann, Opt. Lett. **29**, 468 (2004).
- <sup>2</sup>R. R. Thomson, T. A. Birks, S. G. Leon-Saval, A. K. Kar, and J. Bland-Hawthorn, Opt. Exp. **19**, 5698 (2011).
- <sup>3</sup>A. Zukauskas, M. Malinauskas, C. Reinhardt, B. N. Chichkov, and R. Gadonas, Appl. Opt. **51**, 4995 (2012).
- <sup>4</sup>M. Merker, R. Ackermann, R. Kammel, K. S. Kunert, and S. Nolte, Lasers in Surgery and Medicine **45**, 589 (2013).
- <sup>5</sup>R. Meesata, H. Belmouaddine, J.-F. Allard, C. Tanguay-Renaud, R. Lemay, T. Brastaviceanu, L. Tremblay, B. Paquette, J. R. Wagner, J.-P. Jay-Gerin, M. Lepage, M. A. Huels, and D. Houde, PNAS **109**, E2508 (2012).
- <sup>6</sup>C. Milián, A. Jarnac, Y. Brelet, V. Jukna, A. Houard, A. Mysyrowicz, and A. Couairon arXiv:1405.0438
- <sup>7</sup>R. Stoian, J. P. Colombier, C. Mauclair, G. Cheng, M. K. Buhyan, P. K. Vepula, and P. Srisungitthisunti, Appl. Phys. A **114**, 119 (2014).
- <sup>8</sup>S. Minardi, A. Gopal, M. Tatarakis, A. Couairon, G. Tamōsauskas, R. Piskarskas, A. Dubietis, and P. Di Trapani, Opt. Lett. **33**, 86 (2008).
- <sup>9</sup>S. Minardi, A. Gopal, A. Couairon, G. Tamōsauskas, R. Piskarskas, A. Dubietis, and P. Di Trapani, Opt. Lett. **34**, 3020 (2009).
- <sup>10</sup>A. Couairon, and A. Mysyrowicz, Phys. Rep. **441**, 47 (2007).
- <sup>11</sup>W. J. Jones, and B. P. Stoicheff, Phys. Rev. Lett. **13**, 657 (1964).
- <sup>12</sup>D. Faccio, G. Tamōsauskas, E. Rubino, J. Darginavicius, D.G. Papazoglou, S. Tzortzakis, A. Couairon, and A. Dubietis, Phys. Rev. E **86**, 036304 (2012).
- <sup>13</sup>C. Santhosh, A.K. Dharmadhikari, J.A. Dharmadhikari, K. Alti, and D. Mathur, Appl. Phys. B **99**, 427 (2010).
- <sup>14</sup>D. M. Carey, and G. M. Korenowski, J. Chem. Phys. **108**, 2669 (1998).
- <sup>15</sup>L. A. Rahn, Opt. Lett. **7**, 66 (1981).
- <sup>16</sup>A. Kiraz, S. C. Yorulmaz, M. Yorulmaz, and A. Sennaroglu, Phot. Nanostruct. **7**, 186 (2009).
- <sup>17</sup>see Supplemental material.
- <sup>18</sup>Q. Sun, H. Jiang, Y. Liu, Z. Wu, H. Yang, and Q. Gong, Opt. Lett. **30**, 320 (2005).
- <sup>19</sup>L. V. Keldysh, Sov. Phys. JETP **20**, 1307 (1965).
- <sup>20</sup>P.K. Kennedy, S.A. Boppart, D.X. Hammer, B.A. Rockwell, G.D. Noojin, and W.P. Roach, IEEE J. Quant. El. **31**, 2250 (1995).
- <sup>21</sup>A. Migus, Y. Gauduel, J. L. Martin, and A. Antonetti, Phys. Rev. Lett. **58**, 1559 (1987).
- <sup>22</sup>A. Couairon, E. Brambilla, T. Corti, D. Majus, O.D. Ramirez-Gongora, M. Kolesik, Eur. Phys. J. Special Topics **199**, 5 (2011).
- <sup>23</sup>D. M. Bartels, R. A. Crowell, J. Phys. Chem. A **104**, 3349 (2000).
- <sup>24</sup>A. Bernas, C. Ferradini, J.-P. Jay-Gerin, J. Photochem. Photobiol. A **117**, 171 (1998).